

Article

Terahertz Thermal Sensing by Using a Defect-Containing Periodically Corrugated Gold Waveguide

Jiu-Ling Xue ^{1,2,†}, Lan-Lan Xu ^{1,†}, Tian-Tian Wang ¹, Ya-Xian Fan ^{2,3,*} and Zhi-Yong Tao ^{2,3,*} 

¹ Key Lab of In-Fiber Integrated Optics, Ministry Education of China, Harbin Engineering University, Harbin 150001, China; xuejiuling@hrbeu.edu.cn (J.-L.X.); lanlanxu@hrbeu.edu.cn (L.-L.X.); tiantianwang@hrbeu.edu.cn (T.-T.W.)

² Guangxi Key Laboratory of Wireless Wideband Communication and Signal Processing, Guilin University of Electronic Technology, Guilin 541004, China

³ Academy of Marine Information Technology, Guilin University of Electronic Technology, Beihai 536000, China

* Correspondence: yxfan@guet.edu.cn (Y.-X.F.); zytiao@guet.edu.cn (Z.-Y.T.)

† These authors contributed equally.

Received: 27 May 2020; Accepted: 21 June 2020; Published: 25 June 2020



Featured Application: We used the “COMSOL Multiphysics” software in the simulation process. This software enables the researcher to study the combined effect of a multitude of physical parameters in just one calculation (and for a specific model system). It has unparalleled capabilities, so that all physical phenomena can be perfectly reproduced by using the computer.

Abstract: A terahertz (THz) thermal sensor has been developed by using a periodically corrugated gold waveguide. A defect was positioned in the middle of this waveguide. The periodicities of waveguides can result in Bragg and non-Bragg gaps with identical and different transverse mode resonances, respectively. Due to the local resonance of the energy concentration in the inserted tube, a non-Bragg defect state (NBDS) was observed to arise in the non-Bragg gap. It exhibited an extremely narrow transmission peak. The numerical results showed that by using the here proposed waveguide structure, a NBDS would appear at a resonance frequency of 0.695 THz. In addition, a redshift of this frequency was observed to occur with an increase in the ambient temperature. It was also found that the maximum sensitivity can reach 11.5 MHz/K for an optimized defect radius of 0.9 times the mean value of the waveguide inner tube radius, and for a defect length of 0.2 (or 0.8) times the corrugation period. In the present simulations, a temperature modification of the Drude model was also used. By using this model, the thermal sensing could be realized with an impressive sensitivity. This THz thermal sensor is thereby very promising for applications based on high-precision temperature measurements and control.

Keywords: temperature tunability; defect states; mode interactions; frequency manipulations

1. Introduction

More generally, the terahertz (THz) wave is part of the electromagnetic wave with a frequency range of 0.1–10 THz. Since it is positioned in the transition region of electronics and photonics, its unique characteristics have been found in different types of applications [1,2]. Firstly, as compared with X-rays, the photon energies within this THz region are extremely low. It causes no damage to the living organism and has therefore promising application prospects in the field of biological biopsy [3–5]. Secondly, the wide spectral range of the THz waves can be used to characterize the composition of

matter [6,7]. Thirdly, the THz waves are highly penetrating for many substances, providing a different and more efficient solution for search and rescue [8,9]. Based on these advantages of the THz waves, an increasing number of scientific publications can be found in the field of THz technology. Most of these research activities have focused on THz radiation sources, functional devices, and more practical applications [10–12]. Examples of THz functional devices are filters [13–15], sensors [16,17], slow-light devices [18,19], switches [20,21], absorbers [22], and modulators [23,24].

In recent years, THz sensors have been developed and used in a wide variety of fields. Zhao et al. reported on a broadband THz sensor, based on quantum-cascade laser arrays, which could realize the sensing of the refractive index of solids, or liquids, in a reflective geometry [25]. Yan et al. used THz fiber Bragg gratings to implement the resonant THz sensor, and it was applied to monitor the quality of paper [26]. May et al. proposed a different method for in situ measurement of coating thickness (on individual tablets) during film deposition, by employing a THz line sensor [27]. Zhang et al. presented an ultrasensitive THz sensor, which consisted of a sub-wavelength graphene disk and an annular gold ring within a unit cell. The numerical results showed that a high frequency sensitivity of 1.908 THz, per refractive index unit (RIU), was achieved [28]. Liu et al. took advantage of a thin metal sheet, perforated to a periodic hole array, in constructing a THz surface plasmon sensor that could distinguish the chemical contents in gasoline [29]. In addition, Astley et al. demonstrated a THz multichannel microfluidic sensor that was based on a parallel-plate waveguide with different resonant cavities (two in number). The experimental results showed that the sensitivities of these cavities were 1.21×10^6 nm/RIU and 6.77×10^5 nm/RIU, respectively [30]. Moreover, Vafapour reported on a glucose sensor based on a metamaterial absorber, to be used in food engineering [31]. Islam et al. developed a tunable localized surface plasmon graphene metasurface that should be used as a multiband superabsorber. It will then function as a refractive index sensor for measurements in the surrounding environment [32]. Li et al. reported on a THz metamaterial biosensor, to be used in the measurement of the thermally induced denaturation temperature of insulin [33]. There has also been some research in the field of thermal sensing. For example, Ghafari et al. used the temperature dependencies of the dielectric constants of two materials, graphene and indium antimonide, in the design of a terahertz thermal sensor (with a sensitivity of 160 nm/K) [20]. In terms of patents, Nemirovsky published a patent entitled “Teramos-terahertz thermal sensor and focal plane array” in 2014 [34]. Despite all these earlier investigations in the field of THz sensors, an efficient THz thermal sensor, of a waveguide type, has not yet been reported. This type of sensor is expected to be extremely useful in applications based on high-precision temperature measurements and control.

A THz sensor has been demonstrated in the present study, which is based on a defect-containing periodically corrugated metal tube. This sensor is simple with respect to its structure and has here been found sensitive towards temperature. A Bragg, or a non-Bragg, band gap can be generated when the incident THz wave frequency matches the geometry of the periodic waveguide. By introducing a cylindrical defect in the middle of the periodic structure of the metal tube, the original periodicity will be destroyed. As a result, a defect state will be generated in the former forbidden band. By analyzing the mode components of the defect state, it has here been found that the Bragg defect state consists of almost all first-order modes, while the non-Bragg defect state (NBDS) is dominated by second-order modes. Furthermore, the bandwidth of the NBDS is found to be much narrower (when compared with the Bragg defect state), which makes it more sensitive to changes in ambient temperature. Gold foil’s thermo-optic effect has been studied for a long time. Passian et al. studied the thermally induced multiple photon energy modulations in the surface plasmon of a gold foil [35,36]. The gold waveguide can undergo thermal expansion and contraction, and it propagates the terahertz beam without any leakage. References [37,38] describe in detail the dielectric properties and temperature modulations of gold materials using the Drude model. These characteristics of gold materials, and gold waveguides, are important for the development of a THz thermal sensor in the present study (i.e., by using a periodically corrugated gold waveguide). In the following section (Section 2), the NBDS will be introduced in a periodic metal waveguide by using a defect beyond the traditional Bragg defect

state. In addition, the development of the temperature-modified Drude model will be presented in Section 3, where the thermal sensing of the proposed waveguide structure will also be discussed. In Section 4, the optimization of the waveguide geometry will be presented, and the corresponding sensing performances will be discussed in further detail. Finally, the major results will be summarized in Section 5.

2. NBDSs

Defect states of THz waves in defect-containing periodically corrugated metal tubes can arise not only in the traditional Bragg gap (created by the interaction of two identical transverse modes) but also in a non-Bragg gap (caused by a more complexed resonance). Based on a previous theoretical investigation [39], the non-Bragg resonance refers to the interaction between the different guided transverse modes. Like Bragg resonances, non-Bragg resonances can cause band splitting and form a frequency-forbidden band. However, the characteristics of a non-Bragg forbidden band are completely different from those caused by Bragg resonances. When a defect is introduced into the periodically corrugated metal tube, the defect states can be found to create a transmission peak in the non-Bragg forbidden band.

The defect-containing periodically corrugated gold wave that has been used in the present study is shown in Figure 1. It comprises a periodically corrugated metal tube with a gold thickness of 0.5 μm and a high-density polyethylene (HDPE) of 10 μm thickness. The outer layer of the tube is made of the HDPE, and the inner layer is deposited (i.e., sputtered) with gold. The thickness of the gold layer has been chosen to be 0.5 μm , which is much larger than the skin depth of gold (of around 0.7 THz). Moreover, r_0 , Λ , and Δr represent the mean radius of the inner part of the tube, the wall period, and the corrugation amplitude, respectively. r and z denote a cylindrical coordinate system. A straight tube with a length, L , of 0.8Λ , and a radius, R , of $0.9r_0$, was inserted into the middle of the perfect waveguide. The composition of this structure has earlier been proven to show low loss and dispersion in the THz range, and the refractive index of HDPE is 1.5 [40]. Due to the periodicity of the structure, all dispersion curves (for different transverse modes) were folded back to the first Brillouin zone, where they intersect with each other. Bragg and non-Bragg resonances did also occur in this Brillouin zone, and related frequency gaps appeared. The non-Bragg resonances were created by interactions between the different transverse modes, while the Bragg ones were caused by the same modes in the waveguide [39]. The trends in the dispersion curves, and the frequencies of the resonances, could be predicted by calculating the reference line in the first Brillouin zone:

$$f = \frac{c}{2\pi} \sqrt{\frac{k_r^{(m)^2}}{r_0^2} + \left(\beta + \frac{2m\pi}{\Lambda}\right)^2} \quad (1)$$

where f is the frequency, c is the velocity of light, $k_r^{(m)}$ is the m th zero of the zero-order Bessel function [$\{k_r^{(m)}, m = 1, 2, 3, 4 \dots\} = \{2.4048, 5.5201, 8.6537, 11.7915 \dots\}$], and β ($-\pi/\Lambda \leq \beta \leq \pi/\Lambda$) is the reference propagation constant.

To guarantee the formation of a non-Bragg gap near 0.7 THz, the wall period, Λ , and the mean radius, r_0 , were set to 353 μm and 395.1 μm , respectively (according to Equation (1)). The corrugation amplitude, Δr , of 39.5 μm was then approximately 10% of the mean radius, r_0 . The 2D axisymmetric structure was constructed by using the COMSOL Multiphysics software, with finite element method (FEM) simulations at room temperature ($T = 293$ K). The transmission spectrum of the waveguide is shown by a blue dashed line in Figure 2a. The periodic waveguide has a Bragg gap in the range 0.415–0.560 THz, and a non-Bragg gap in the range 0.610–0.715 THz. For the situation with a straight tube inserted into the middle of the perfect waveguide, the resulting transmission spectrum is demonstrated by a red solid line in Figure 2a. As shown in Figure 2a, a transmission peak appears in each forbidden band, and the Bragg and non-Bragg gaps are split by these induced defect states. The peak frequency of the Bragg defect state is 0.462 THz, and that of NBDS is 0.695 THz. As compared

with the Bragg defect state, the width of the transmission peak for the NBDS is much narrower. This indicates that the characteristics of the NBDS are completely different from those of the Bragg defect state (it is well-known that a non-Bragg gap is created by the involvement of high-order modes). As demonstrated in Figure 1b,c, the magnetic field distributions (H_ϕ) of the Bragg gap state and NBDS show that each defect state is caused by a local resonance, with its origin in the energy concentrations of the THz waves in the inserted tube. This type of local resonance will, hence, induce a longitudinal accumulation of each defect state. However, the radial distribution is different, which is caused by the involvement of high-order transverse modes in the NBDS. Due to the rotation symmetry with respect to the z-axis, Figure 1b,c denotes any shaft sections.

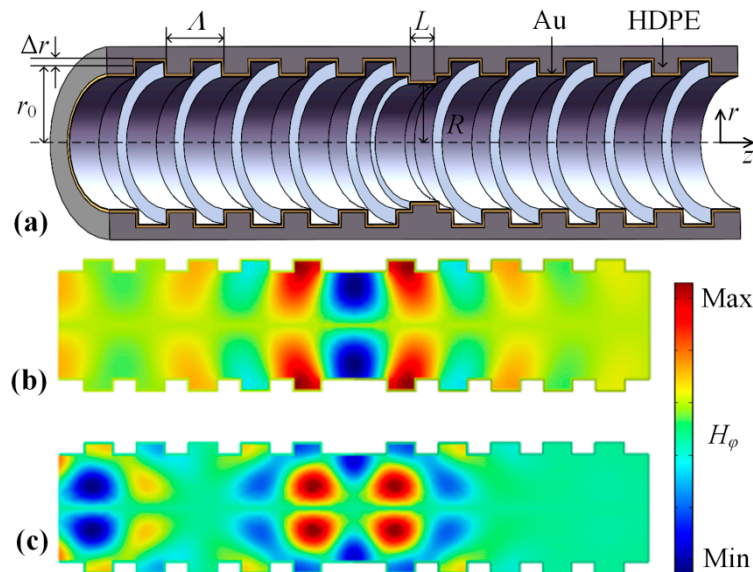


Figure 1. (a) Configurations of the proposed waveguide. The middle straight pipe contains the defect structure, where L and R are the length and the radius of the defect, respectively. (b) The magnetic field distribution at the peak frequency (0.462 THz) of the Bragg defect state. (c) The magnetic field distribution (H_ϕ) at the peak frequency (0.695 THz) of the non-Bragg defect state (NBDS).

The magnetic field distributions of the defect states were also investigated (as can be seen in Figure 2b). The underlying reason was to study the effect of different transverse modes on the NBDSs. The longitudinal location of a specific radius, r , was selected at the maximum (absolute) value of the amplitude in the waveguide. There is one radius of this kind in the Bragg defect state, but two in the NBDS. To quantitatively identify the mode components of the defect states, a least-square fit to the radial distributions was utilized:

$$H_\phi(r) = \sum_{m=1}^4 a_m J_1(k_r^{(m)} r) \quad (2)$$

where r represents the radius (normalized by its own maximum), a_m denotes the coefficients of the different transverse modes, and $J_1(\cdot)$ is the first-order Bessel function. The best fitting curves for the Bragg and non-Bragg defect states are shown in blue vs. red in Figure 2b. The optimal coefficients for the Bragg defect state are $a_1 = 1.1810$, $a_2 = 0.0232$, $a_3 = -0.0012$, and $a_4 = 0.0001$, while these are $a_1 = 0.1369$, $a_2 = 1.0960$, $a_3 = -0.0145$, and $a_4 = 0.0148$ for the NBDS. Thus, it is obvious that the first mode plays a major role for the Bragg defect state, while the other modes are all sufficiently small. It is the other way around for the NBDS, for which the second mode dominates (as compared with the others). In fact, this second mode is essential for the major characteristics of the NBDS.

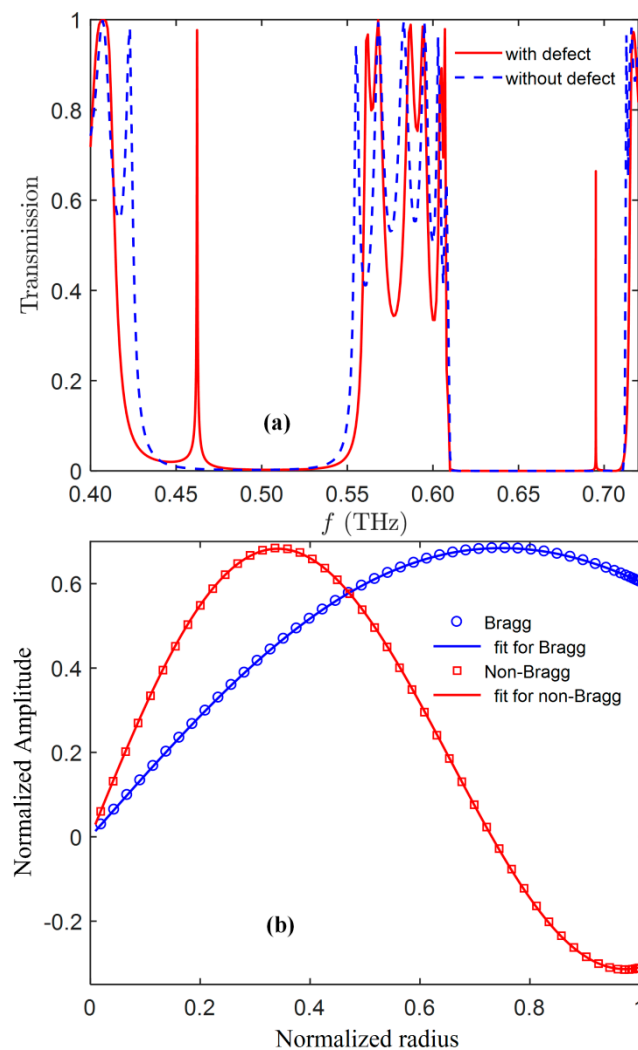


Figure 2. (a) Comparison of Bragg and non-Bragg stop-bands, with and without defects: red solid line = transmission curve for the waveguide with defects; blue dashed line = transmission curve for the waveguide without defects. (b) Radial distributions for the Bragg and non-Bragg defect states: red squares = normalized magnetic field strengths for the NBDS; blue circles = normalized magnetic field strengths for the Bragg defect state. The blue and red solid lines show the best fitting curves.

In short, by introducing a straight tube into a periodically corrugated waveguide, longitudinal accumulation with local resonances was the result. This is quite different from the Bragg defect state and is a very promising way to achieve a sensor with much higher sensitivity. The use of NBDS is thus very promising and can be applied in various types of THz sensing systems, such as ambient temperature monitoring.

3. Thermal Sensing

In the development of a temperature sensor, one must consider the thermal expansion of the waveguide material (Au in this case). Thus, when the temperature is changed, the geometry of the proposed waveguide will also change. Consequently, the THz response of the waveguide material will vary by changing the temperature. Thus, the frequency of the NBDS will shift according to the varying temperature, which can be directly used to sense temperature changes. With the linear expansion

coefficient of Au, α , the period, Λ , and mean radius, r_0 , of the proposed waveguide, the following temperature dependencies can be obtained:

$$\Lambda(T) = (1 + \alpha\Delta T)\Lambda \tag{3}$$

$$r_0(T) = (1 + \alpha\Delta T)r_0 \tag{4}$$

where the temperature difference, ΔT , is the deviation from room temperature, 293 K.

In addition, the traditional Drude model must be modified because of the temperature dependency of the THz response. The well-known Drude conductivity formula is shown in Equation (5).

$$\sigma(0) = \frac{\omega_p^2}{\omega_\tau} \epsilon_0 \tag{5}$$

where $\sigma(0)$ is the DC conductivity, ϵ_0 is the dielectric constant in vacuum, ω_p is the plasma frequency, and ω_τ is the damping frequency. Furthermore, ω_p and ω_τ are defined as

$$\begin{cases} \omega_p = \sqrt{\frac{q(-e)^2}{\epsilon_0 m}} \\ \omega_\tau = \frac{1}{\tau} \end{cases} \tag{6}$$

where q is the number of conducting electrons per unit volume, e is the charge of the electron, m is the electron mass, and τ is the relaxation time [37]. Moreover, the electric conductivity, $\sigma(\omega)$, can be given by

$$\sigma(\omega) = \frac{\sigma(0)}{1 - i\omega\tau} \tag{7}$$

where the circular frequency $\omega = 2\pi f$. The complex dielectric constant in the Drude model, $\epsilon = \epsilon_1 + i\epsilon_2$, is also expressed as

$$\begin{cases} \epsilon_1 = 1 - \frac{\omega_p^2}{\omega^2 + \omega_\tau^2} \\ \epsilon_2 = \frac{\omega_p^2 \omega_\tau}{\omega^3 + \omega \omega_\tau^2} \end{cases} \tag{8}$$

where $\omega_p = 1.37 \times 10^4$ THz, and $\omega_\tau = 40.7$ THz (for Au) [38].

For a temperature close to room temperature, the Drude model of the dielectric constant can be modified to become dependent on the temperature. At first, assume that Equations (5)–(8) are valid at room temperature, $T_0 = 293$ K. It is then possible to study the temperature dependency as a function of the variation in T , ΔT (when close to room temperature). For isotropic materials, the thermally induced expansion (in volume) yields the temperature-dependent electron density, $q/(1 + 3\alpha\Delta T)$. This is due to the small value of the expansion coefficient, α . The temperature-dependent plasma frequency, $\omega_p(T)$, can therefore be calculated by using Equation (9).

$$\omega_p(T) = \frac{\omega_p}{\sqrt{1 + 3\alpha\Delta T}} \tag{9}$$

According to the quantum theories of electrons for pure metals, the damping frequency, ω_τ , is linearly dependent on the temperature in the high-temperature range (i.e., over the Debye temperature). For this high-temperature range, the temperature-dependent damping frequency, $\omega_\tau(T)$, will be linearly dependent on ω_τ : $\omega_\tau(T) \propto \omega_\tau$. Since the electrical resistivity is the inverse of the DC conductivity, it is also proportional to the temperature. Thus, the damping frequency can be modified as:

$$\omega_\tau(T) = \omega_\tau \frac{1 + \alpha_R \Delta T}{1 + 3\alpha \Delta T} \tag{10}$$

where α_R is the temperature coefficient of the resistivity at T_0 .

Considering the temperature modified Drude model, and the thermal expansion of Au, various parameters were set in the RF module of COMSOL Multiphysics. These parameters include the temperature-dependent dielectric constant of Au, as well as the period and radius for different temperatures. For the NBDS, simulated results for different temperatures are shown in Figure 3. As can be seen in this figure, as the temperature increases, the transmission peaks gradually shift to lower frequencies. Additionally, the width of the peaks becomes wider, and the transmittances will gradually decrease. The frequency shift is, thus, a very promising parameter to measure in the determination of the temperature variation in the environment (i.e., for sensing). More generally, the sensitivity and the figure of merit (FOM) are two important parameters that reflect the performance of a sensor. The definition of sensitivity can be expressed as $\Delta f/\Delta T$, where Δf is the frequency shift of the transmission peak and ΔT is the numerical shift in temperature. By applying this definition of sensitivity on the results presented in Figure 3, it is obvious that the sensitivity of this THz thermal sensor can reach 11.5 MHz/K. Moreover, according to reference [41], the FOM of a terahertz thermal sensor is the ratio of the sensitivity to the full width at half maximum (FWHM): $\text{FOM} = (\text{Sensitivity} \times T)/\text{FWHM}$. The FOM of the here presented waveguide-based thermal sensor has a maximum value of 142.7 (at $T = 273$ K), which is larger than the FOM of 117, as presented in Ref. [39]. As shown in Figure 3, the FWHM of the transmission peaks increases sharply with an increase in temperature. This makes FOM smaller, but it can still reach a FOM value of 28.9 (at $T = 353$ K). The observation that FOM becomes smaller as the temperature rises is a problem to be solved in the near future. The most important result is, though, that we have constructed a waveguide-based THz thermal sensor by measuring the frequencies of the transmission peaks.

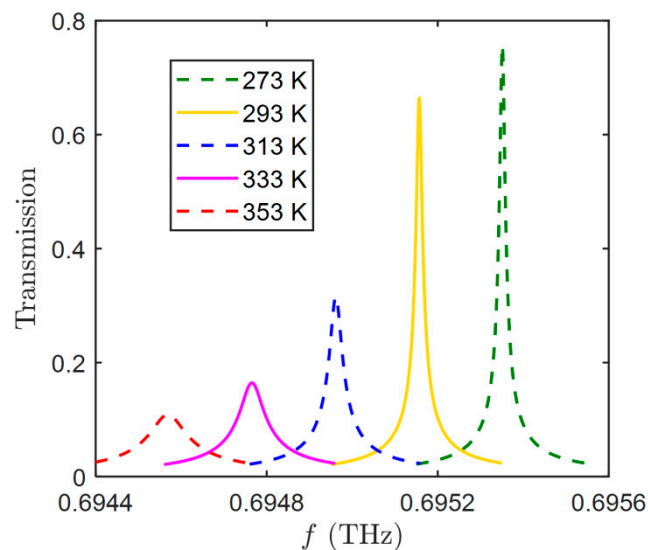


Figure 3. Frequency shifts of the NBDS when the temperature is increased from 273 K to 353 K.

4. Sensing Performances

To adjust the tunable temperature-related characteristics of the here proposed THz thermal sensor, the defect parameters have been further investigated by using simulations. It has been observed that by changing the length and radius of the defect, the peak frequency of the NBDS will shift accordingly. At first, the defect length L was set to 0.5Λ , and the defect radius, R , was varied from $0.3r_0$ to $1.1r_0$. The variations in transmission frequency, as a function of temperature, are shown in Figure 4a. The results are presented for different defect radius, R (from $0.3r_0$ to $1.1r_0$). To make Figure 4a more intuitive, the transmission frequency, f , value for $R = 0.7r_0$ and $T = 313$ K has been set to zero, and the other f values have been accordingly adjusted (i.e., these f values are reported with respect to the one for $R = 0.7r_0$ and $T = 313$ K). As can be seen in Figure 4a, for a constant temperature, the transmission frequency, f , will increase with an increase in defect radius, R . For the situation with a constant defect

radius, the frequency will continuously decrease when increasing the temperature from 273 K to 353 K. To obtain the sensitivity of the proposed thermal sensor, a least square linear fit has been performed for each set of simulated data. The sensitivity, averaged over the five different sets, was then found to be 9.35 ± 0.80 MHz/K. The highest sensitivity was found for $R = 0.7r_0$, with a value of 10.15 MHz/K.

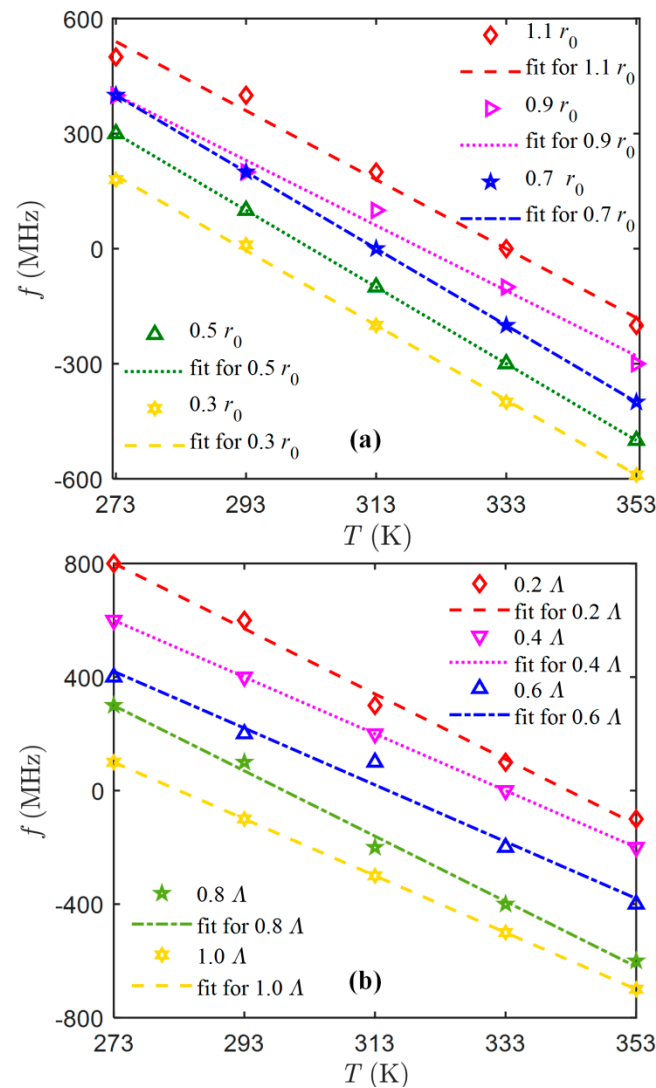


Figure 4. Structure optimization of the proposed THz thermal sensor. Frequency shifts for different defect radii, R (a), and different defect lengths, L (b).

The next step was to study the effect of various defect lengths, L , (0.2Λ , 0.4Λ , 0.6Λ , 0.8Λ , and 1.0Λ) for a constant defect radius, R , (of $0.9r_0$). Simulations were thereby performed at temperatures, T , that were increased from 273 K to 353 K (in steps of 20 K). The obtained frequency deviations are shown in Figure 4b (by using the transmission peak for $L = 0.6\Lambda$, at 313 K, as a reference). In this figure, it can be seen that the transmission peak shifts to a lower frequency as the defect length, L , increases (at constant T). Moreover, at a constant defect length, the frequency decreases with an increase in temperature. The sensitivity, averaged over the five different sets, was found to be 10.75 ± 0.75 MHz/K. Moreover, the highest sensitivity was found for both $L = 0.2\Lambda$ and $L = 0.8\Lambda$, with a value of 11.5 MHz/K.

5. Conclusions

A THz thermal sensor, based on a defect-containing periodic waveguide, has been proposed in the present investigation. This periodic THz waveguide is found to exhibit a non-Bragg band gap in a specific frequency range. When a defect is introduced in the structure, a defect state can be formed in the non-Bragg band gap (called NBDS). The spectrum of a waveguide, with a defect in the THz frequency range, is also simulated. As a result, it is found that the resonance frequency of the NBDS can be controlled by varying the temperature, which, in turn, is due to the thermal expansion of the metal structure in the waveguide. It is found that the NBDS will move to lower frequencies as the temperature rises. In addition, the Drude model has to be modified since the temperature is varied. It is found that not only the thermal expansion, but also the dielectric constant, will influence the THz thermal sensing. The temperature-modified Drude model is observed to efficiently estimate the THz response of metals at various ambient temperatures. Furthermore, the geometry of the implemented defect is also investigated in the study of the sensing performances. It is thereby found that when the defect length increases, the transmission peak will gradually shift to lower frequencies. On the contrary, the transmission peak will shift to higher frequencies when the radius is increased. In summary, the combination of a tunable defect size, high sensitivity, and ease in operation, of the here proposed structure in the THz regime, makes this temperature sensor very promising for applications based on high-precision temperature measurements and control.

Author Contributions: Conceptualization, Y.-X.F. and Z.-Y.T.; validation, J.-L.X., L.-L.X., and T.-T.W.; formal analysis, L.-L.X., Y.-X.F., and Z.-Y.T.; writing—original draft preparation, J.-L.X., L.-L.X., and T.-T.W.; writing—review and editing, Y.-X.F. and Z.-Y.T.; visualization, L.-L.X., and T.-T.W.; supervision, Y.-X.F. and Z.-Y.T. All authors have read and agreed to the published version of the manuscript.

Funding: This research was funded by the Dean Project of Guangxi Key Laboratory of Wireless Broadband Communication and Signal Processing, the National Natural Science Foundation of China (11374071), and the Natural Science Foundation of Heilongjiang Province, China (QC2018001).

Conflicts of Interest: The authors declare no conflict of interest.

References

1. Siegel, P.H. Terahertz Technology. *IEEE Trans. Microw. Theory Tech.* **2002**, *50*, 910–928. [[CrossRef](#)]
2. Lee, M.; Wanke, M.C. Searching for a Solid-State Terahertz Technology. *Science* **2007**, *316*, 64–65. [[CrossRef](#)] [[PubMed](#)]
3. Nishizawa, J.I.; Sasaki, T.; Suto, K.; Yamada, T.; Tanabe, T.; Tanno, T.; Sawai, T.; Miura, Y. THz imaging of nucleobases and cancerous tissue using a GaP THz-wave generator. *Opt. Commun.* **2005**, *244*, 469–474. [[CrossRef](#)]
4. Siegel, P.H. Terahertz Technology in Biology and Medicine. *IEEE Trans. Microw. Theory Tech.* **2004**, *52*, 2438–2447. [[CrossRef](#)]
5. Zhang, R.; He, Y.; Liu, K.; Zhang, L.; Zhang, S.; Pickwell-MacPherson, E.; Zhao, Y.; Zhang, C. Composite multiscale entropy analysis of reflective terahertz signals for biological tissues. *Opt. Express* **2017**, *25*, 23669–23676. [[CrossRef](#)]
6. Peretti, R.; Braud, F.; Peytavit, E.; Dubois, E.; Lampin, J.F. Broadband Terahertz Light–Matter Interaction Enhancement for Precise Spectroscopy of Thin Films and Micro-Samples. *Photonics* **2018**, *5*, 11. [[CrossRef](#)]
7. Vegni, A.M.; Loscrí, V. Characterization and performance analysis of a chiral-metamaterial channel with Giant Optical Activity for terahertz communications. *Nano Commun. Netw.* **2016**, *9*, 28–35.
8. Miao, Q.; Wang, G.; Li, Y.J. Research of Landmine Detection Using Terahertz Technology. *Appl. Mech. Mater.* **2014**, *644*, 1313–1316. [[CrossRef](#)]
9. Samluk, J.P.; Schuetz, C.A.; Dillon, T.; Stein, E.L.; Robbins, A.; MacKrides, D.G.; Martin, R.D.; Wilson, J.; Chen, C.; Prather, D.W. Q-Band Millimeter Wave Imaging in the Far-Field Enabled by Optical Upconversion Methodology. *J. Infrared Milli. Terahz. Waves* **2012**, *33*, 54–66. [[CrossRef](#)]
10. Wang, D.; Liu, J. Polarization property of the THz wave generated from a two-color laser-induced gas plasma. *Phys. Rev. A* **2012**, *86*, 023833. [[CrossRef](#)]

11. Ito, H.; Furuta, T.; Nakajima, F.; Yoshino, K.; Ishibashi, T. Photonic Generation of Continuous THz Wave Using Uni-Travelling-Carrier Photodiode. *J. Light. Technol.* **2005**, *23*, 4016–4021. [[CrossRef](#)]
12. Hübers, H.W. Towards THz integrated photonics. *Nat. Photonics* **2010**, *4*, 503. [[CrossRef](#)]
13. Xu, L.L.; Tao, Z.Y.; Sang, T.Q.; Xu, D.; Wang, P.F.; Fan, Y.X. Thermally Tunable Narrow Band Filter Achieved by Connecting Two Opaque Terahertz Waveguides. *IEEE Photonics Technol. Lett.* **2017**, *29*, 869–872. [[CrossRef](#)]
14. Zhang, B.; Wu, Q.; Pan, C.; Feng, R.; Xu, J.; Lou, C.; Wang, X.; Yang, F. THz band-stop filter using metamaterials surfaced on LiNbO₃ sub-wavelength slab waveguide. *Opt. Express* **2015**, *23*, 16042–16051. [[CrossRef](#)]
15. Lin, Z.; Xu, Z.; Liu, P.; Liang, Z.; Lin, Y. Polarization-sensitive terahertz resonator using asymmetrical F-shaped metamaterial. *Opt. Laser Technol.* **2020**, *121*, 105826. [[CrossRef](#)]
16. Stantchev, R.I.; Phillips, D.B.; Hobson, P.; Hornett, S.M.; Padgett, M.J.; Hendry, E. Compressed sensing with near-field THz radiation. *Optica* **2017**, *4*, 989–992. [[CrossRef](#)]
17. Ding, C.; Jiang, L.; Wu, L.; Gao, R.; Xu, D.; Zhang, G.; Yao, J. Dual-band ultrasensitive THz sensing utilizing high quality Fano and quadrupole resonances in metamaterials. *Opt. Commun.* **2015**, *350*, 103–107. [[CrossRef](#)]
18. Zhao, J.; Song, J.; Zhou, Y.; Zhao, R.; Zhou, J. Tunable multiple plasmon-induced transparency in a simple terahertz Dirac semimetal based metamaterial. *Opt. Mater. Express* **2019**, *9*, 3325–3332. [[CrossRef](#)]
19. Amemiya, T.; Yamasaki, S.; Tanaka, M.; Kagami, H.; Masuda, K.; Nishiyama, N.; Arai, S. Demonstration of slow-light effect in silicon-wire waveguides combined with metamaterials. *Opt. Express* **2019**, *27*, 15007–15015. [[CrossRef](#)]
20. Ghafari, S.; Forouzeshefard, M.R.; Vafapour, Z. Thermo Optical Switching and Sensing applications of an Infrared metamaterial. *IEEE Sens. J.* **2020**, *20*, 3235–3241. [[CrossRef](#)]
21. Amin, M.; Farhat, M.; Bağcı, H. A dynamically reconfigurable Fano metamaterial through graphene tuning for switching and sensing applications. *Sci. Rep.* **2013**, *3*, 02105. [[CrossRef](#)] [[PubMed](#)]
22. Alves, F.; Karamitros, A.; Grbovic, D.; Kearney, B.; Karunasiri, G. Highly absorbing nano-scale metal films for terahertz applications. *Opt. Eng.* **2012**, *51*, 063801. [[CrossRef](#)]
23. Liu, X.; Chen, Z.; Parrott, E.P.J.; Ung, B.S.Y.; Xu, J.; Pickwell-MacPherson, E. Graphene Based Terahertz Light Modulator in Total Internal Reflection Geometry. *Adv. Opt. Mater.* **2017**, *5*, 1600697. [[CrossRef](#)]
24. Yan, R.; Sensale-Rodriguez, B.; Liu, L.; Jena, D.; Xing, H.G. A new class of electrically tunable metamaterial terahertz modulators. *Opt. Express* **2012**, *20*, 28664–28671. [[CrossRef](#)]
25. Zhao, L.; Khanal, S.; Wu, C.; Kumar, S. Proposal for a broadband THz refractive-index sensor based on quantum-cascade laser arrays. *Opt. Express* **2015**, *23*, 4751–4765. [[CrossRef](#)]
26. Yan, G.; Chinifooroshan, Y.; Tripathi, S.M.; Bock, W.J.; Skorobogatiy, M. Resonant THz sensor for paper quality monitoring using THz fiber Bragg gratings. *Opt. Lett.* **2013**, *38*, 2200–2202. [[CrossRef](#)]
27. May, R.K.; Evans, M.J.; Zhong, S.; Warr, I.; Gladden, L.F.; Shen, Y.; Zeitler, J.A. Terahertz In-Line Sensor for Direct Coating Thickness Measurement of Individual Tablets During Film Coating in Real-Time. *J. Pharm. Sci.* **2011**, *100*, 1535–1544. [[CrossRef](#)]
28. Zhang, Y.; Li, T.; Zeng, B.; Zhang, H.; Lv, H.; Huang, X.; Zhang, W.; Azad, A.K. A graphene based tunable terahertz sensor with double Fano resonances. *Nanoscale* **2015**, *7*, 12682–12688. [[CrossRef](#)]
29. Liu, G.; He, M.; Tian, Z.; Li, J.; Liu, J. Terahertz surface plasmon sensor for distinguishing gasolines. *Appl. Opt.* **2013**, *52*, 5695–5700. [[CrossRef](#)]
30. Astley, V.; Reichel, K.S.; Jones, J.; Mendis, R.; Mittleman, D.M. Terahertz multichannel microfluidic sensor based on parallel-plate waveguide resonant cavities. *Appl. Phys. Lett.* **2012**, *100*, 231108. [[CrossRef](#)]
31. Vafapour, Z. Polarization-independent perfect optical metamaterial absorber as a glucose sensor in Food Industry applications. *IEEE Trans. Nanobiosci.* **2019**, *18*, 622–627. [[CrossRef](#)]
32. Islam, M.S.; Sultana, J.; Biabanifard, M.; Vafapour, Z.; Nine, M.J.; Dinovitsner, A.; Cordeiro, C.M.B.; Ng, B.W.-H.; Abbott, D. Tunable localized surface plasmon graphene metasurface for multiband superabsorption and terahertz sensing. *Carbon* **2020**, *158*, 559–567. [[CrossRef](#)]
33. Li, D.; Lin, S.; Hu, F.; Chen, Z.; Zhang, W.; Han, J. Metamaterial Terahertz Sensor for Measuring Thermal-Induced Denaturation Temperature of Insulin. *IEEE Sens. J.* **2020**, *20*, 1821–1828. [[CrossRef](#)]
34. Nemirovsky, Y. Teramos-Terahertz Thermal Sensor and Focal Plane Array. U.S. Patent 8759776B2, 24 June 2014.
35. Passian, A.; Lereu, A.L.; Arakawa, E.T.; Wig, A.; Thundat, T.; Ferrell, T.L. Modulation of multiple photon energies by use of surface plasmons. *Opt. Lett.* **2005**, *30*, 41–43. [[CrossRef](#)] [[PubMed](#)]
36. Passian, A.; Lereu, A.L.; Ritchie, R.H.; Meriaudeau, F.; Thundat, T.; Ferrell, T.L. Surface plasmon assisted thermal coupling of multiple photon energies. *Thin Solid Films* **2006**, *497*, 315–320. [[CrossRef](#)]

37. Mizutani, U. *Introduction to the Electron Theory of Metals*; Cambridge University Press: Cambridge, UK, 2001; p. 249.
38. Ordal, M.A.; Long, L.L.; Bell, R.J.; Bell, S.E.; Bell, R.R.; Alexander, R.W.; Ward, C.A. Optical properties of the metals Al, Co, Cu, Au, Fe, Pb, Ni, Pd, Pt, Ag, Ti and W in the infrared and far infrared. *Appl. Opt.* **1983**, *22*, 1099–1120. [[CrossRef](#)]
39. Zhang, L.; Fan, Y.X.; Liu, H.; Xu, L.L.; Xue, J.L.; Tao, Z.Y. Hypersensitive and Tunable Terahertz Wave Switch Based on Non-Bragg Structures Filled with Liquid Crystals. *J. Light. Technol.* **2017**, *35*, 3092–3098. [[CrossRef](#)]
40. Chen, X.; Ma, M.; Yang, X.; Yang, K.; Liu, D.; Ji, T.; Wu, S.; Zhu, Z. Optical properties of carbon materials filled HPDE composites in THz region. *Nucl. Sci. Tech.* **2009**, *20*, 265–270.
41. Ma, Y.; Nguyen-Huu, N.; Zhou, J.; Maeda, H.; Wu, Q.; Eldlio, M.; Pištora, J.; Cada, M. Mach-Zehnder Interferometer-based Integrated Terahertz Temperature Sensor. *IEEE J. Sel. Top. Quantum Electron.* **2017**, *23*, 4601607. [[CrossRef](#)]



© 2020 by the authors. Licensee MDPI, Basel, Switzerland. This article is an open access article distributed under the terms and conditions of the Creative Commons Attribution (CC BY) license (<http://creativecommons.org/licenses/by/4.0/>).